Electronic Supplementary Information

Electrochemical Carbon Dioxide Reduction on Copper-Zinc Alloys: Ethanol and Ethylene Selectivity Analysis

Yeji Baek‡[a], Hakhyeon Song‡[a], Deokgi Hong‡[b], Suneon Wang[a], Sungwoo Lee[bc], Young-Chang Joo[bcd], Gun-Do Lee*[bc], and Jihun Oh*[a]*

[a] Department of Materials Science and Engineering, Korea Advanced Institute of Science and Technology (KAIST), 291, Daehak-ro, Yuseong-gu, Daejeon 34141, Republic of Korea

[b] Department of Materials Science and Engineering, Seoul National University, 1, Gwanak-ro, Gwanak-gu, Seoul 08826, Republic of Korea

[c] Research Institute of Advanced Materials (RIAM), Seoul National University, 1, Gwanak-ro, Gwanak-gu, Seoul 08826, Republic of Korea

[d] Advanced Institute of Convergence Technology, 145, Gwanggyo-ro, Yeongtong-gu, Suwon-si, Gyeonggi-do 16229, Republic of Korea

‡ These authors contributed equally to this work.

*Corresponding Authors E-mails: ycjoo@snu.ac.kr; gdlee@snu.ac.kr; jihun.oh@kaist.ac.kr

Experimental Details

Electrode Preparation: Bimetallic CuZn alloys were deposited by magnetron sputtering on carbon paper (39BB, Sigracet) or a polytetrafluoroethylene membrane (pore size: 0.45 μm, Sterlitech). The Cu (99.998%, iTasco) and Zn (99.999%, iTasco) sputtering targets were powered by direct current (DC) and radio frequency (RF), respectively. Cu and/or Zn were co-deposited for 10 min at different deposition powers. The composition ratio of the CuZn alloys was adjusted by controlling the RF power (20, 40, and 60 W) of Zn, while maintaining a constant DC power of Cu (100 W).

Electrode Characterization: The material characterization of Cu and CuZn alloys was performed using the following techniques: scanning electron microscopy (SEM, Magellan 400, FEI company), X-ray diffraction (XRD, D/MAX-2500, Rigaku) with Cu-Kα radiation, X-ray photoelectron spectroscopy (XPS, K-alpha, Thermo VG Scientific and Axis-Supra, Kratos), ultraviolet photoelectron spectroscopy (UPS, Axis-Supra, Kratos) with a helium gas energy of 21.2 eV (He I) and Ar^+ ion etching, inductively coupled plasma mass spectrometry (ICP-MS, Agilent ICP-MS 7700S, Agilent), and scanning transmission electron microscopy with energy dispersive X-ray spectroscopy (STEM-EDX, Cs-corrected STEM, JOEL, 200 kV). The double-layer capacitance method was used to measure the electrochemically active surface area (ECSA) of Cu and CuZn alloys. Double-layer capacitance was obtained by measuring the difference in the charging and discharging current densities in the range of ± 40 mV based on the open-circuit potential, at cyclic voltammetry (CV) scan rates of 75, 100, 125, 150, and 200 mV/s in a mixed solution of K_2CO_3 and $KHCO_3$ to set the pH to 10. An electrochemical OH^- absorption study was conducted by performing CV (100 mV/s) in 1 M KOH with N_2 flow.

Electrochemical measurements: The electrochemical CO_2 reduction reaction was carried out in a microfluidic gas-diffusion electrode (GDE) reactor. CuZn alloys on a carbon paper and a NiFeMo foil (80:15:4.2 wt%, 0.102 mm, Alfa Aesar) were used as the working electrode and counter electrode, respectively. The geomaterial areas of the working and counter electrodes for CO_2RR were 2 cm^2. Around 8.5 mL of 1 M KOH was used as the catholyte and anolyte. Ag/AgCl with saturated KCl (RE-1B, EC-Frontier) was used as the reference electrode and was calibrated periodically for precise measurements. The catholyte and anolyte were separated by a Sustainion membrane (Sustainion X37-50 RT, Dioxide Materials). The catholyte was circulated using a peristaltic liquid pump (Masterflex L/S pump) at a flow rate of 12 mL/min, from a 50 mL reservoir of 1 M KOH . The anolyte reservoirs were circulated under the same conditions at high current densities. CO_2 (99.999%) was delivered into the gas chamber of the GDE reactor at a total flow rate of 20 sccm using mass flow controllers (MFC, MFC KOREA). Deionized water (DI water, 18.2 MΩ·cm resistivity) from a Millipore water purifier and KOH (ACS Reagent, Merck) were used to minimize impurities.

Chronoamperometry (CA) for CO_2 electrolysis was carried out for 20 min after the stabilization of the potential for 5 min, using potentiostats (SP-150 and VSP/VMP3B-5, Biologic) with software IR compensation of 85% uncompensated resistance (R_u). Gaseous CO_2RR products, such as H_2, CO, CH_4, and C_2H_4, were detected in situ using gas chromatography (GC, Youngin Chromass) with a thermal conductivity detector (TCD) and flame ionization detector (FID). Liquid products such as $HCOO^-$ and CH_3COO^- were collected after CO_2RR, and characterized by high performance liquid chromatography (HPLC) with a Hi-Plex H column (Agilent) after 10 times dilution and neutralizing KOH solution with 0.5 M H_2SO_4 or 1 M HCl. Additionally, alcohols, including CH_3OH, C_2H_5OH, and C_3H_7OH, were quantified by

headspace GC, using the same detectors. CO_2RR performance was analyzed using three samples to ensure reproducibility. The potential applied to the working electrode is expressed on a reversible hydrogen electrode (RHE) scale:

$$\text{Potential (V vs. RHE)} = \text{Potential (V vs. Ag/AgCl)} + 0.197 + 0.0591 \times \text{pH} \quad (1)$$

The FE of CO_2RR products were calculated using the following equation:

$$\text{FE}\ (\%) = z \cdot n \cdot F / Q \quad (2)$$

where z is the number of electrons transferred, n is the number of moles of product formed based on the outlet flow rate, F is Faraday's constant, and Q is the amount of charge passed.

A membrane electrode assembly (MEA) of 5 cm^2 was purchased from Dioxide Materials. A piece of Cu_9Zn_1/PTFE (3 cm × 3 cm) was attached to the cathodic side with a hand-made copper tape frame (2.2 × 2.2 cm) and a PTFE gasket for electrical connection. The Sustainion membrane (Sustainion X37-50 RT, Dioxide Materials) and Ni mesh (100 mesh, woven from 0.1 mm, Alfa aesar) were used as the anion exchange membrane and anode, respectively. On the anode side, 1 M KOH electrolyte was circulated by a peristaltic liquid pump at a flow rate of 10 mL/min. On the cathode side, humidified CO_2 (a mixture of CO_2 and DI water) was supplied at a flow rate of 100 sccm. Pre-electrolysis was carried out at −0.25 A for 20 min under the same CO_2RR conditions, before CO_2 electrolysis at −0.5 A for 7 h.

In the MEA system, the full-cell energy efficiency (EE) of ethanol was calculated using the following equation:

$$\text{EE}\ (\%) \text{ of ethanol} = (1.23 + (-E_{\text{ethanol}})) \times \text{FF}_{\text{ethanol}} / -E_{\text{full cell}} \quad (3)$$

where $E_{ethanol}$ and $E_{full\text{-}cell}$ are the standard reduction potential and full-cell voltage applied, respectively.

DFT calculations: DFT calculations were performed within the generalized gradient approximation (GGA) of the Perdew–Burke–Ernzerhof (PBE) functional[1] using the Vienna ab initio simulation package (VASP).[2,3] The plane-wave basis had an energy cut-off of 400 eV. The Brillouin zone was sampled using a 3 × 3 × 1 Monkhorst-Pack mesh. Structural optimization was performed until the force on each atom was less than 0.01 eV/Å. A 3 × 3 four-layer slab of Cu (100) and a 3 × 4 four-layer slab of Cu (111) were modelled, and the vacuum space was set to 15 Å to avoid interactions with their periodic images. The DFT-D3 method in Grimme's scheme was applied to describe the van der Waals (vdW) interactions[4]. For electrochemical reactions involving the proton-coupled electron transfer step, free energies of the reaction were calculated based on a computational hydrogen electrode model.[5,6]

Figure S1. Cross-sectional and plane-view scanning electron microscopy (SEM) images of (a) Cu, (b) thick Cu, and (c) Cu_2Zn_1.

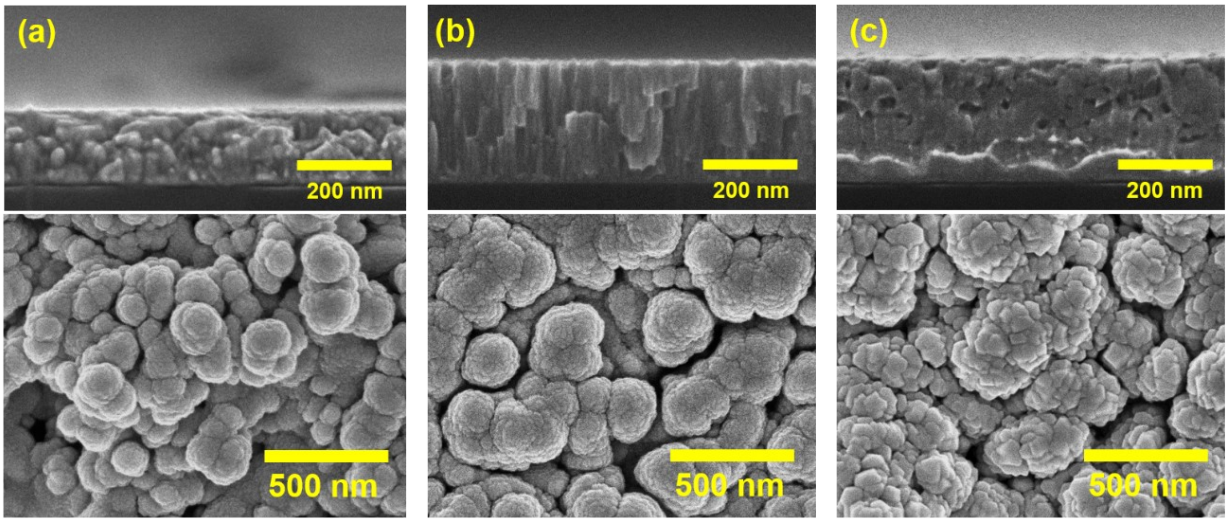

Figure S2. (a, e and i) SEM images and scanning electron microscopy with energy-dispersive X-ray spectroscopy (SEM-EDS) mappings of (b, f and j) overlap, (c, g and k) Cu and (d, h and l) Zn elements before electrochemical CO_2 reduction reaction (CO_2RR): (a-d) Cu_9Zn_1, (e-h) Cu_3Zn_1, and (i-l) Cu_2Zn_1 alloys.

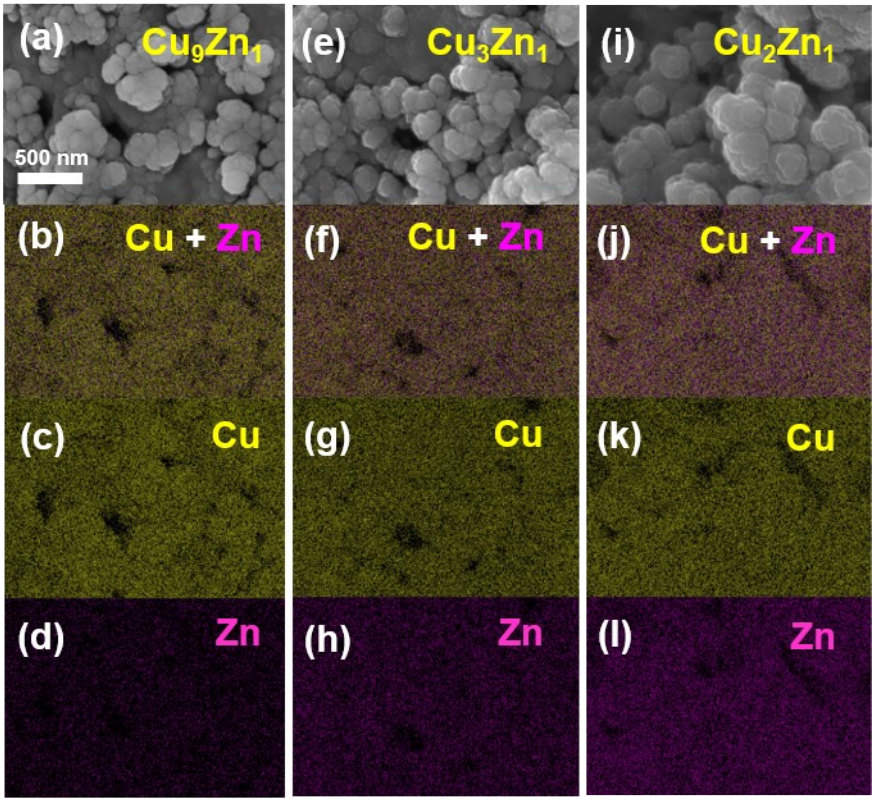

Figure S3. (a) Transmission electron microscopy (TEM) image, (b) scanning transmission electron microscopy (STEM) image, (c-e) scanning transmission electron microscopy with energy dispersive X-ray spectroscopy (STEM-EDS) mapping and (f) high-resolution transmission electron microscopy (HR-TEM) image of Cu_3Zn_1 before CO_2RR.

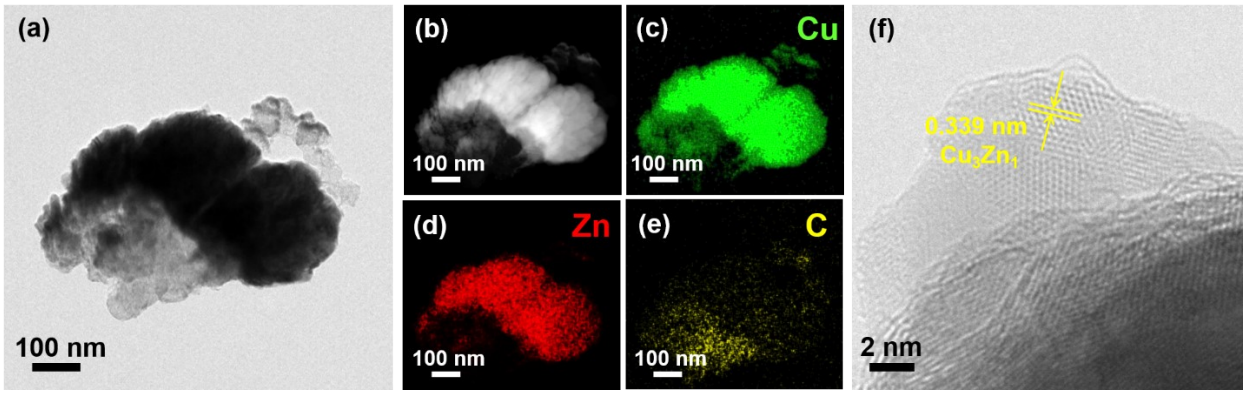

Figure S4. X-ray diffraction (XRD) patterns of CuZn alloys on carbon paper.

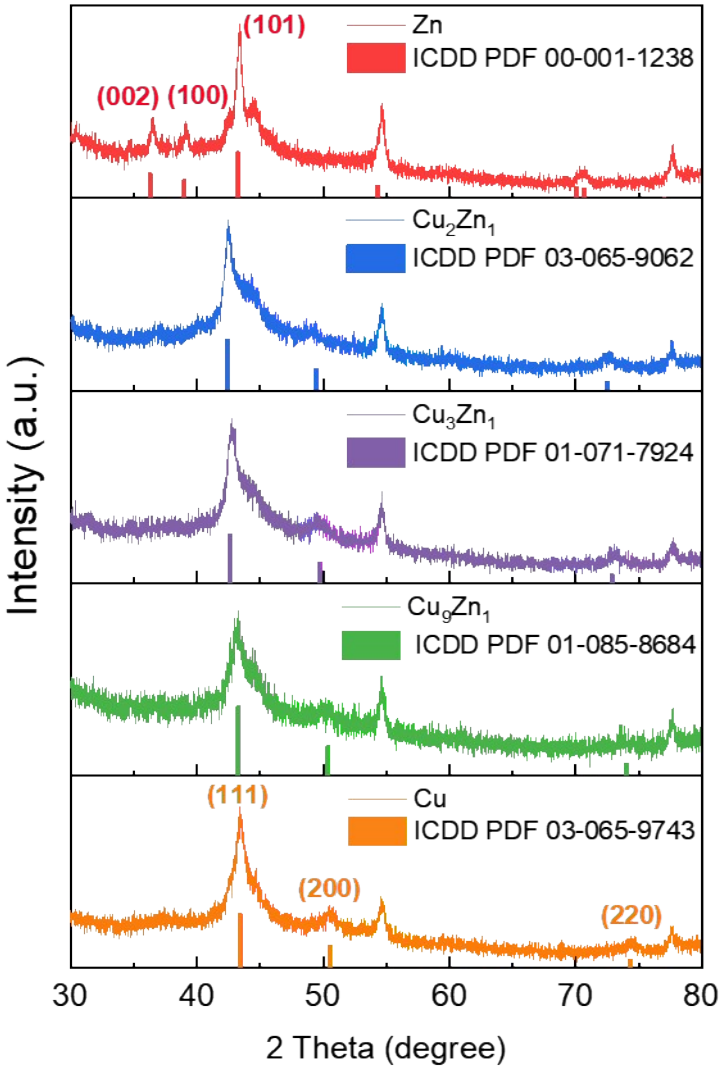

Figure S5. XRD patterns of carbon paper.

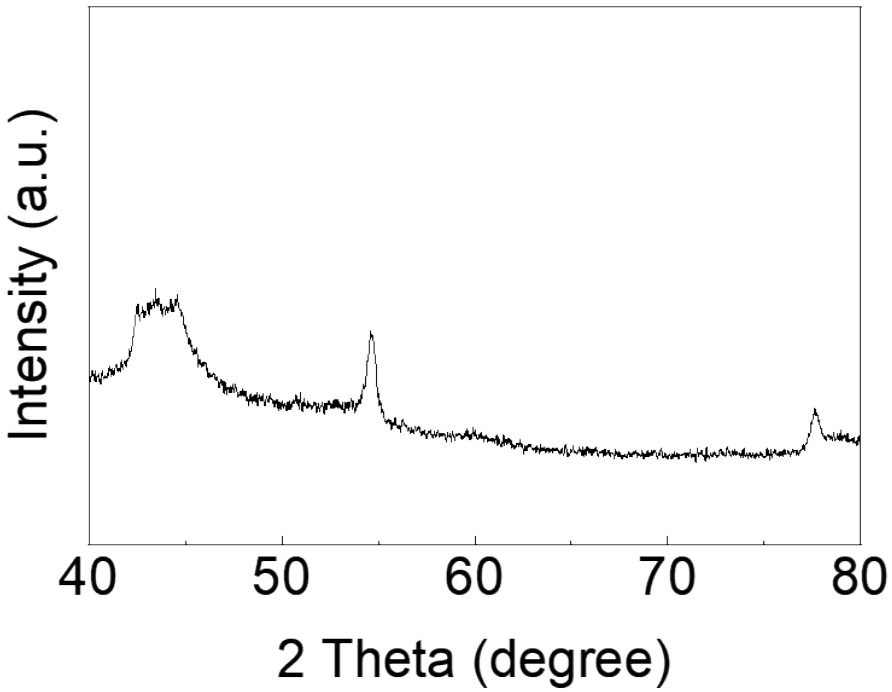

Figure S6. OH^- absorption peaks in cyclic voltammetry scans on (a) Cu, and (b) Cu_2Zn_1

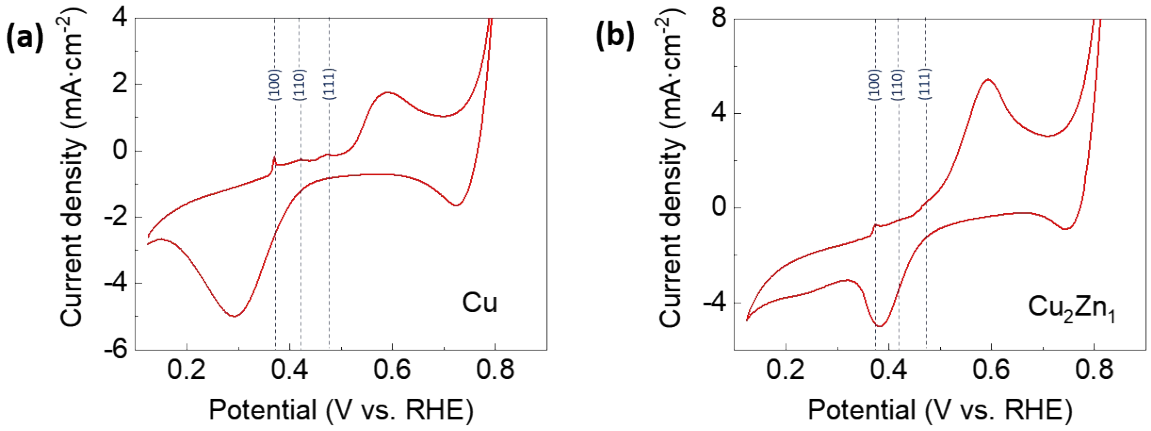

Figure S7. Lattice parameter, actual Zn composition and calculated Zn composition based on Vegard's law.

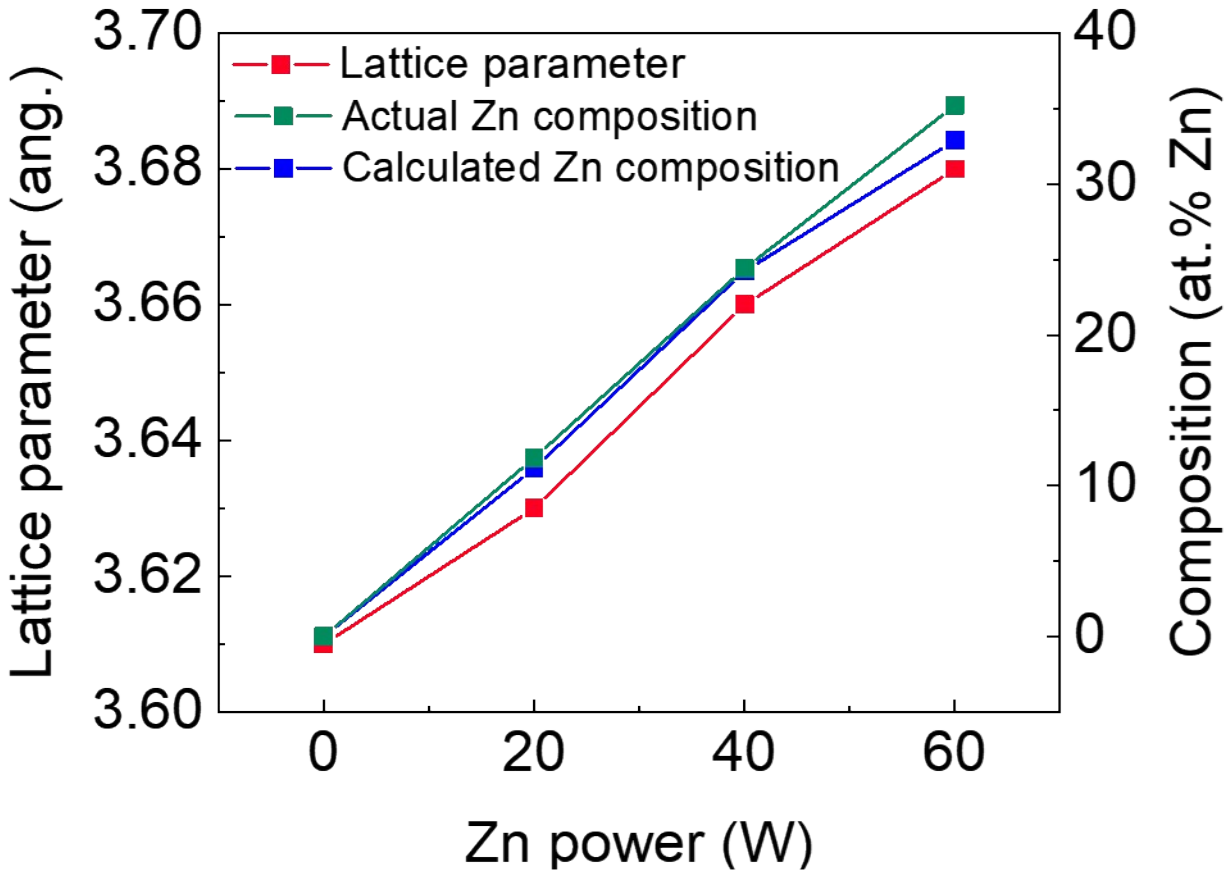

Figure S8. Cu X-ray photoelectron spectroscopy (XPS) spectra of Cu and CuZn alloys (a) before CO_2RR, (b) after CO_2RR at −0.9 V vs. RHE, and (c) after CO_2RR at −1 V vs. RHE.

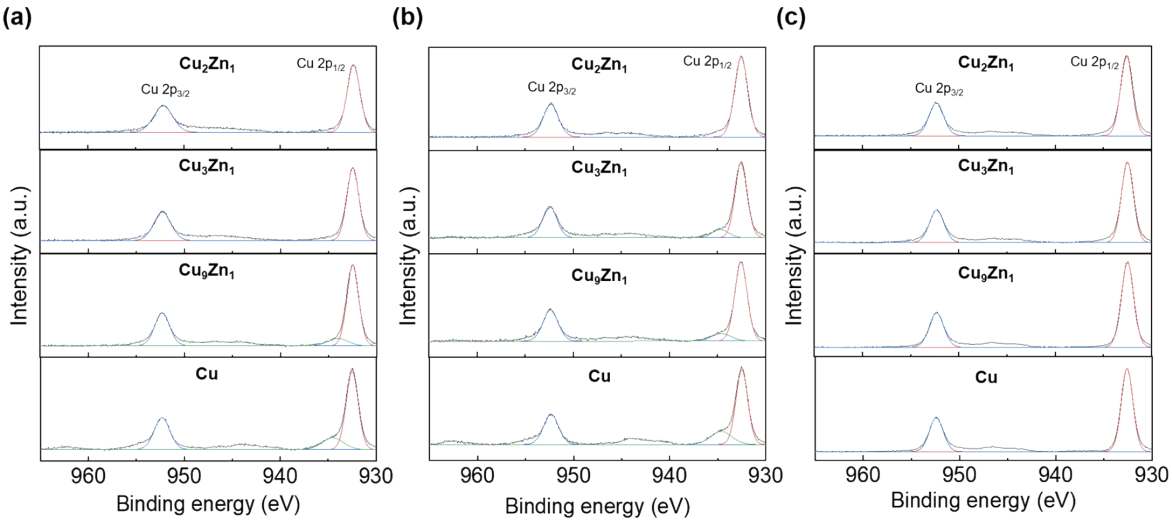

Figure S9. Zn XPS spectra of Cu and CuZn alloys (a) before CO_2RR, (b) after CO_2RR at −0.9 V vs. RHE, and (c) after CO_2RR at −1 V vs. RHE.

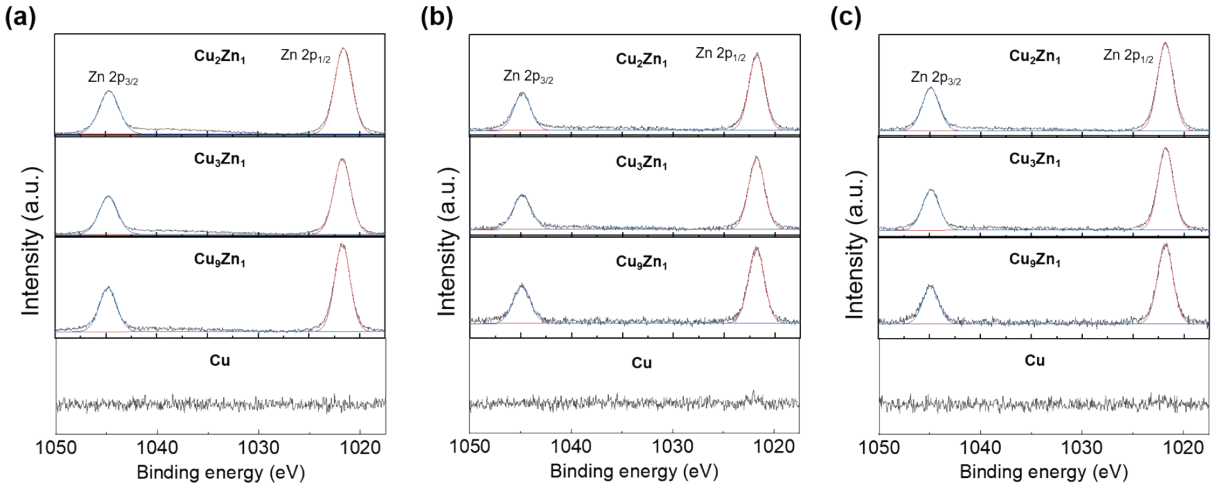

Figure S10. Surface and bulk composition of Zn before and after CO_2RR as a function of Zn sputtering power.

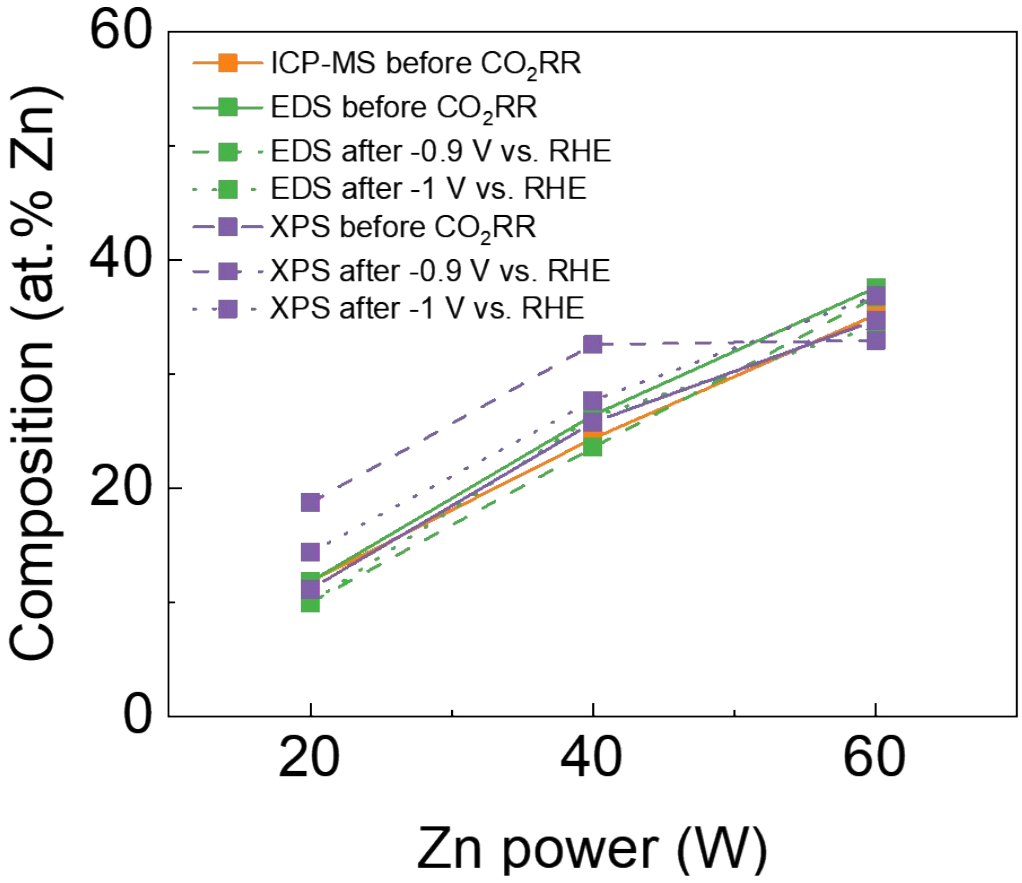

Figure S11. SEM images of Cu and CuZn alloys after CO_2RR at (a) −0.9 V vs. RHE, and (b) −1 V vs. RHE.

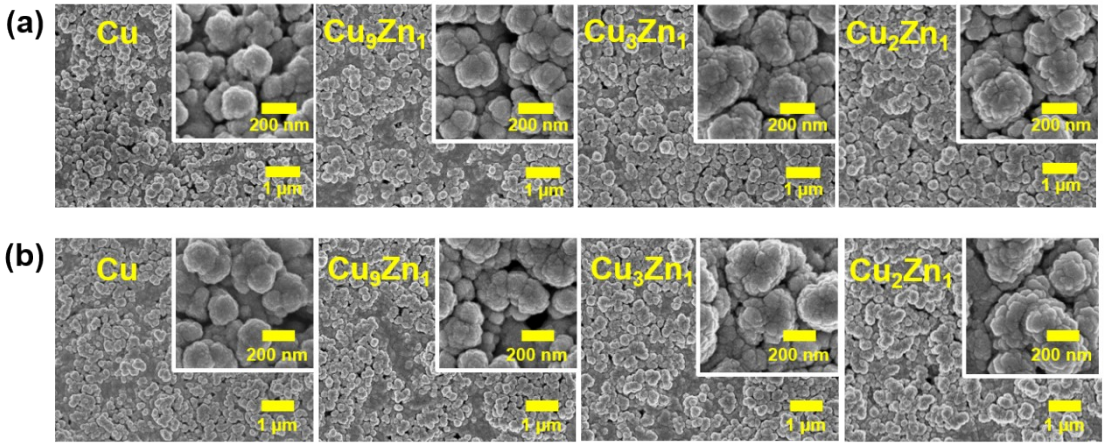

Figure S12. (a, e and i) SEM images and SEM-EDS mapping of (b, f and j) overlap, (c, g and k) Cu and (d, h and l) Zn elements after CO_2RR at -0.9 V vs. RHE: (a-d) Cu_9Zn_1, (e-h) Cu_3Zn_1 and (i-l) Cu_2Zn_1 alloys.

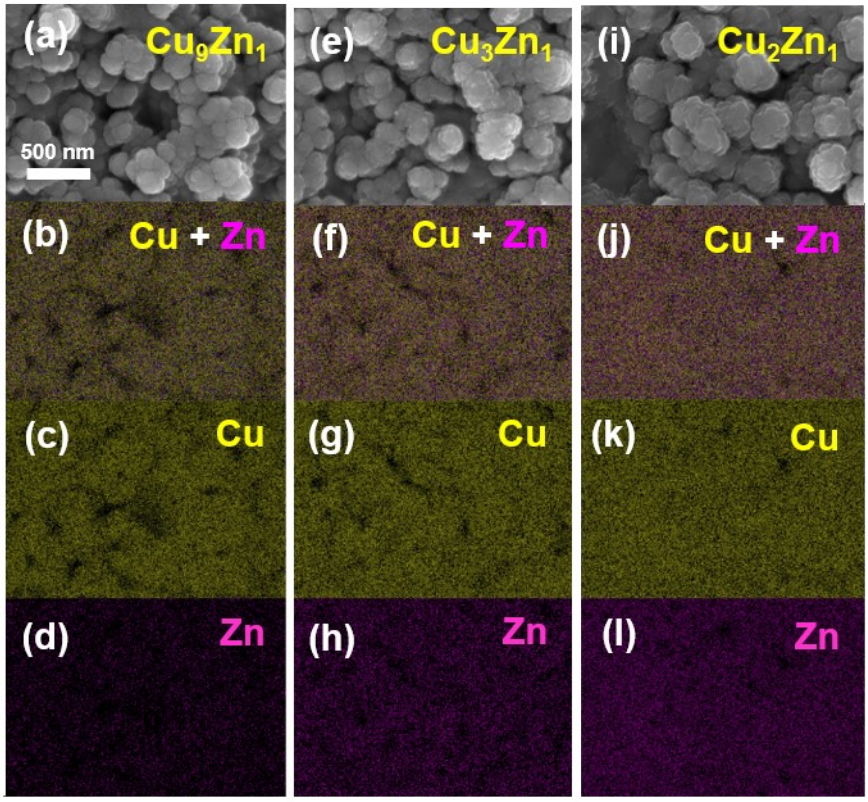

Figure S13. (a, e and i) SEM images and SEM-EDS mapping of (b, f and j) overlap, (c, g and k) Cu and (d, h and l) Zn elements after CO_2RR at -1 V vs. RHE: (a-d) Cu_9Zn_1, (e-h) Cu_3Zn_1 and (i-l) Cu_2Zn_1 alloys.

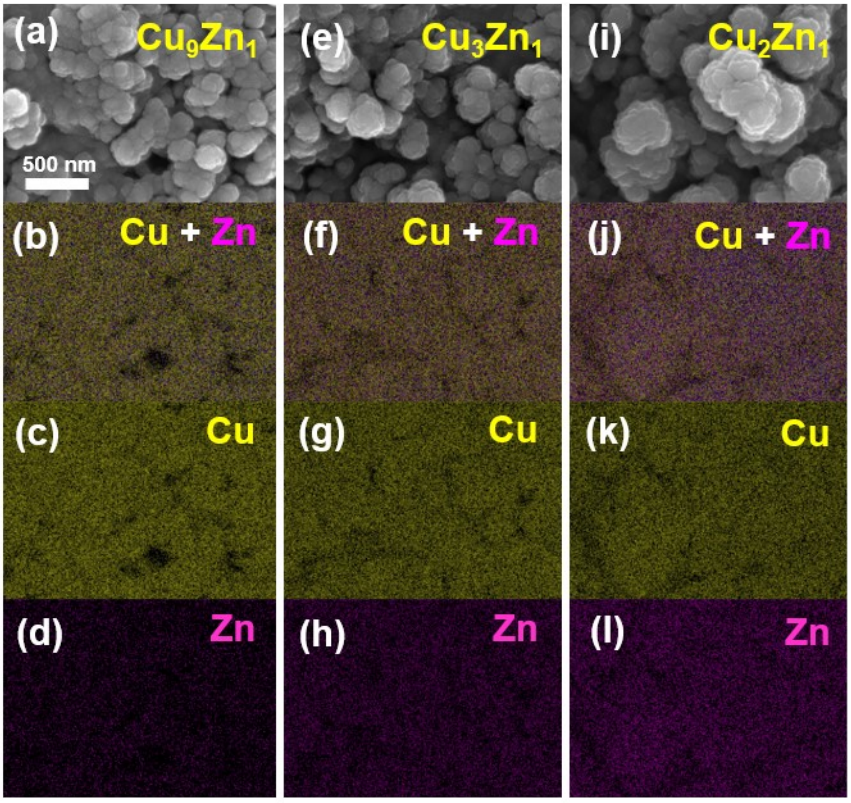

Figure S14. XRD patterns of (a) Cu, (b) Cu_9Zn_1, (c) Cu_3Zn_1, and (d) Cu_2Zn_1 before and after CO_2RR.

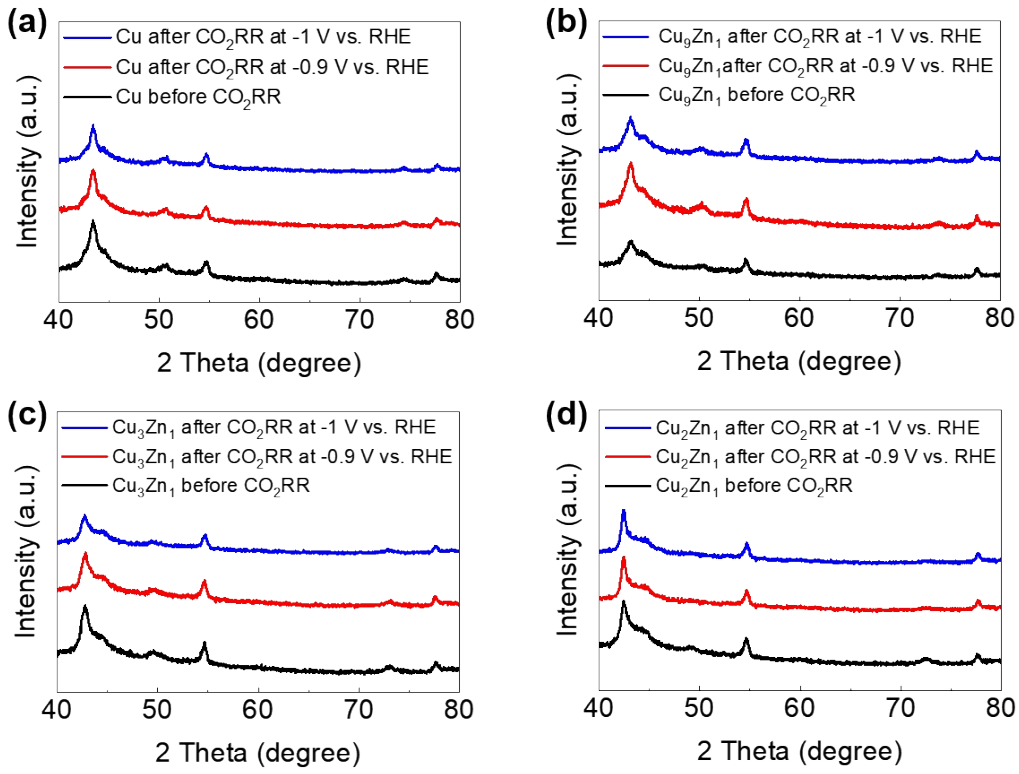

Figure S15. (a-b) TEM images, (c) STEM image, and (d-f) STEM-EDS mapping of Cu_3Zn_1 after CO_2RR.

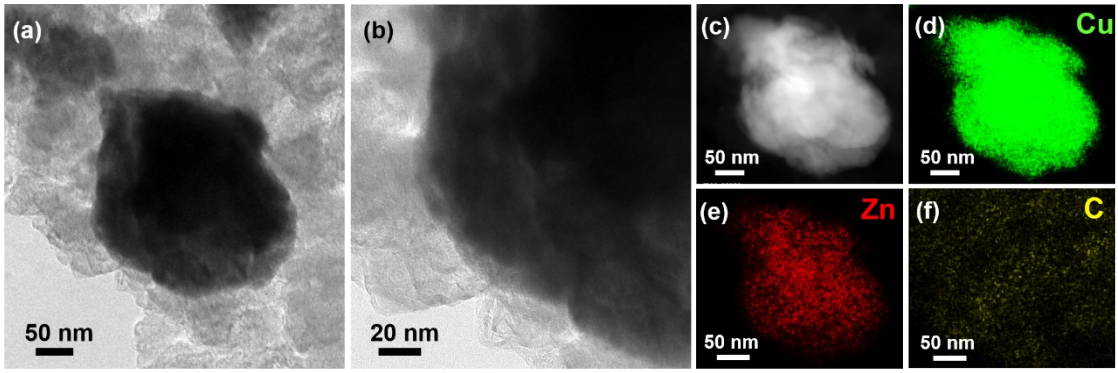

Figure S16. Total and CO_2RR current density normalized by (a) geometric area and (b) electrochemically active surface area. (c) Consumed CO_2 normalized by geometric area and electrochemically active surface area as a function of Zn composition at −0.9 V vs. RHE.

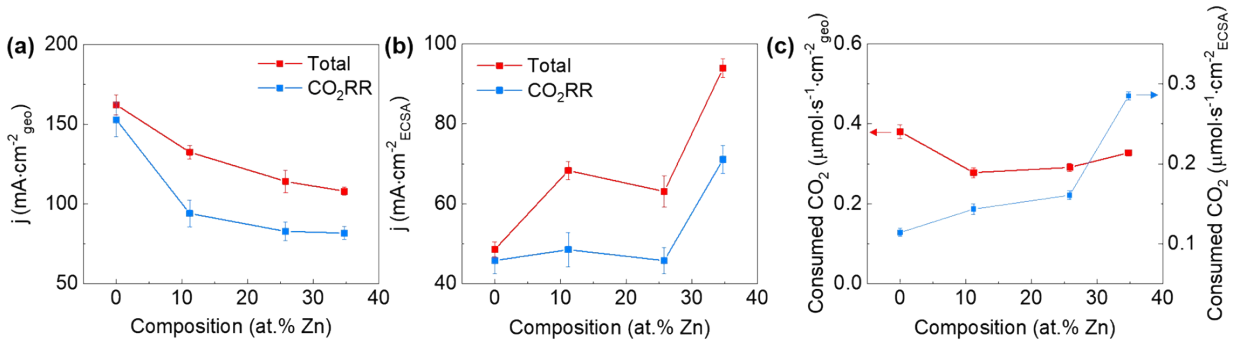

Figure S17. Cyclic voltammetry scans for (a) flat Cu on silicon wafer, (b) Cu, (c) Cu_9Zn_1, (d) Cu_3Zn_1, and (e) Cu_2Zn_1 on carbon paper at various scan rates. (f) Linear fitting between current density and scan rate.

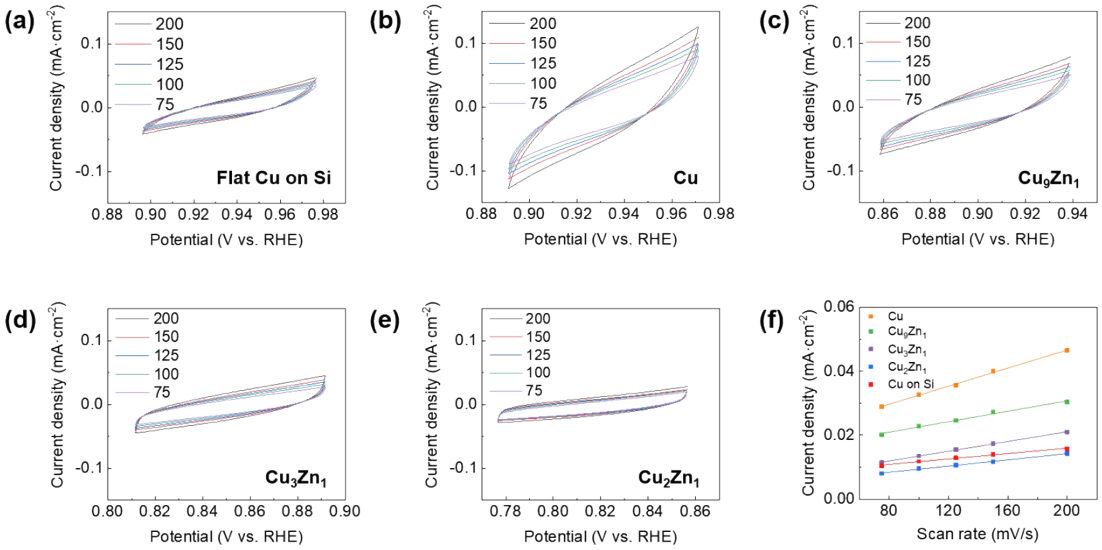

Table S1. Double-layer capacitance and electrochemically active surface area of Cu and CuZn alloys.

Samples	Capacitance ($\mu F/cm^2$)	Electrochemically active surface area (cm^2)
Flat Cu on Si	42.3	2
Cu	141	6.68
Cu_9Zn_1	81.9	3.87
Cu_3Zn_1	76.4	3.61
Cu_2Zn_1	48.8	2.31

Figure S18. Partial current densities of major products from CO_2RR normalized by (a) geometric area and (b) electrochemically active surface area as function of Zn composition at −1 V vs. RHE.

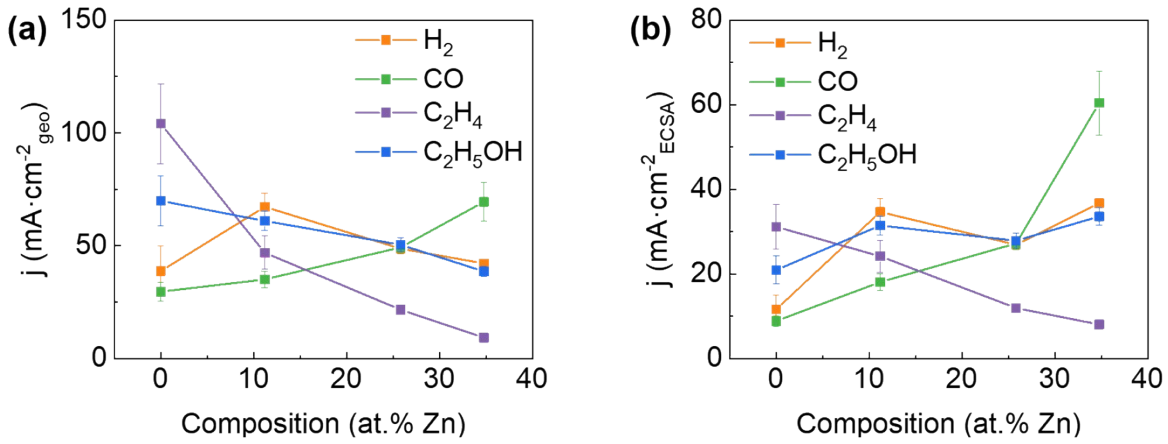

Figure S19. Partial current densities normalized by (a) geometric area and (b) electrochemically active surface area and (c) Faradaic efficiencies of major products from CO_2RR as a function of Zn composition at −0.9 V vs. RHE.

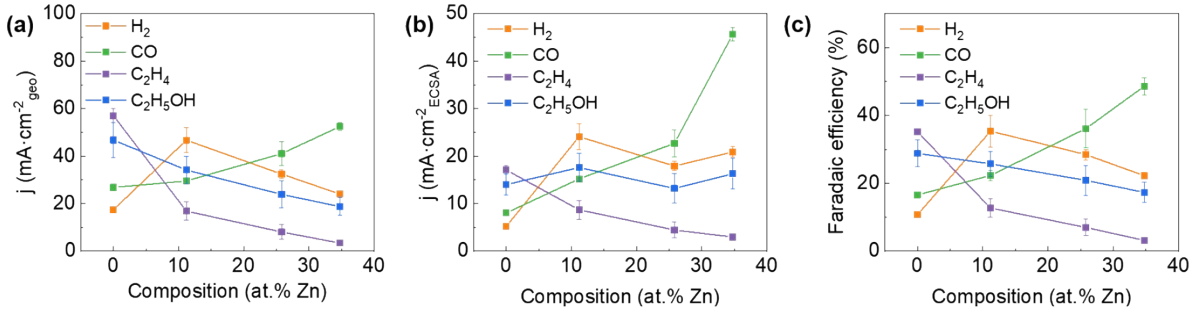

Table S2. Faradaic efficiencies of all products from CO_2RR on Cu and CuZn catalysts

Catalyst	Potential (V vs. RHE)	H_2	CO	C_2H_4	C_2H_5OH	C_3H_7OH	CH_4	CH_3OH	$HCOO^-$	Total
Cu	-0.9	10.71	16.55	35.17	28.80	3.76	2.24	2.64	4.50	104.37
	-1	14.36	11.12	38.95	26.19	2.98	3.40	1.77	2.66	101.43
Cu_9Zn_1	-0.9	35.35	22.31	12.70	25.72	2.54	0.95	3.38	2.97	105.91
	-1	28.80	15.09	20.02	26.23	1.67	1.48	2.23	1.47	96.98
Cu_3Zn_1	-0.9	28.44	36.13	6.97	20.86	2.61	0.69	3.43	1.52	100.64
	-1	25.15	25.44	11.19	26.05	1.69	1.48	3.00	0.89	94.88
Cu_2Zn_1	-0.9	22.23	48.62	3.14	17.30	1.50	0.42	3.02	1.37	97.60
	-1	23.80	39.16	5.23	21.78	1.10	1.19	2.54	1.17	95.98

Figure S20. Faradaic efficiencies of all products from electrolysis with N_2 and CO_2 flow on Cu_2Zn_1 catalyst in 1 M KOH, at −1 V vs. RHE.

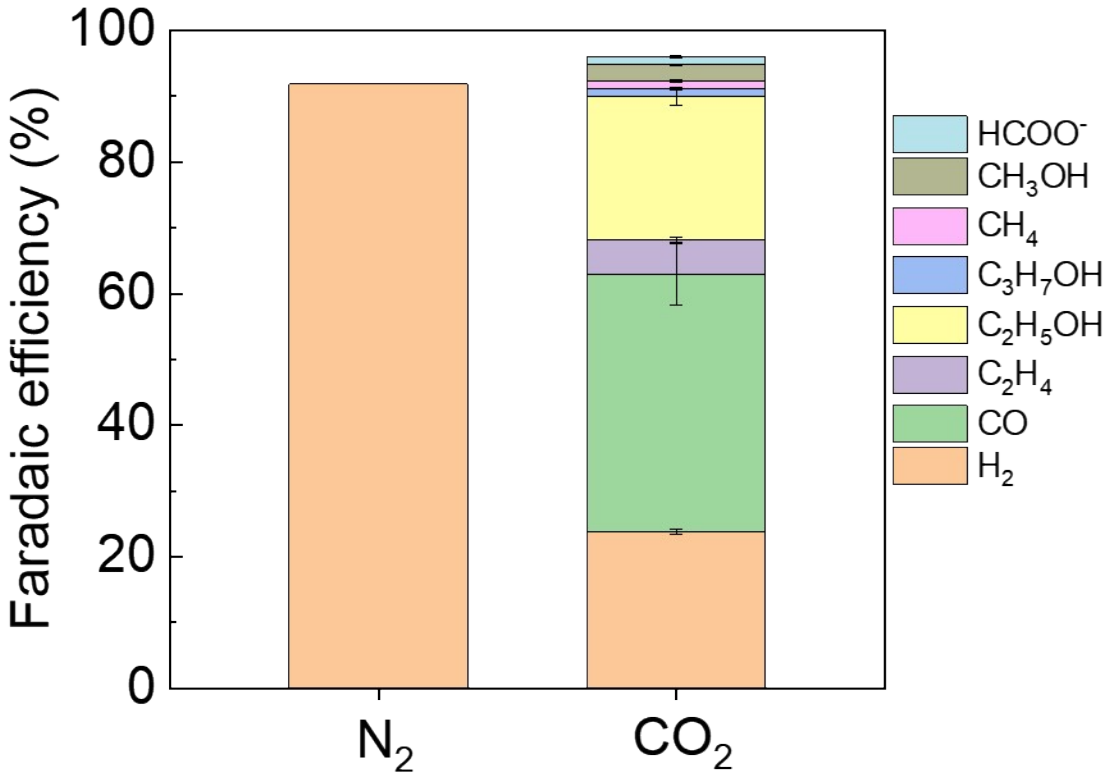

Figure S21. Potential-dependent total current density and Faradaic efficiencies of major products from CO_2RR on Zn catalyst.

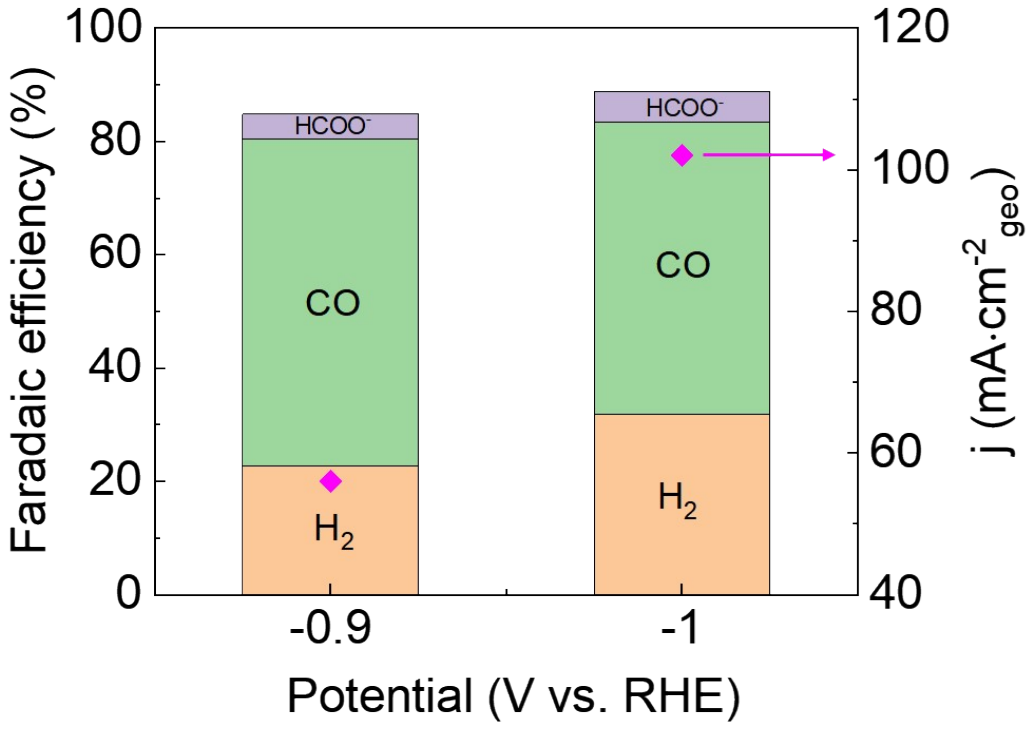

Figure S22. Zn composition-dependent C_2H_5OH/C_2H_4 ratio and partial current density of C_{2+} products normalized by electrochemically active surface area at −0.9 V vs. RHE.

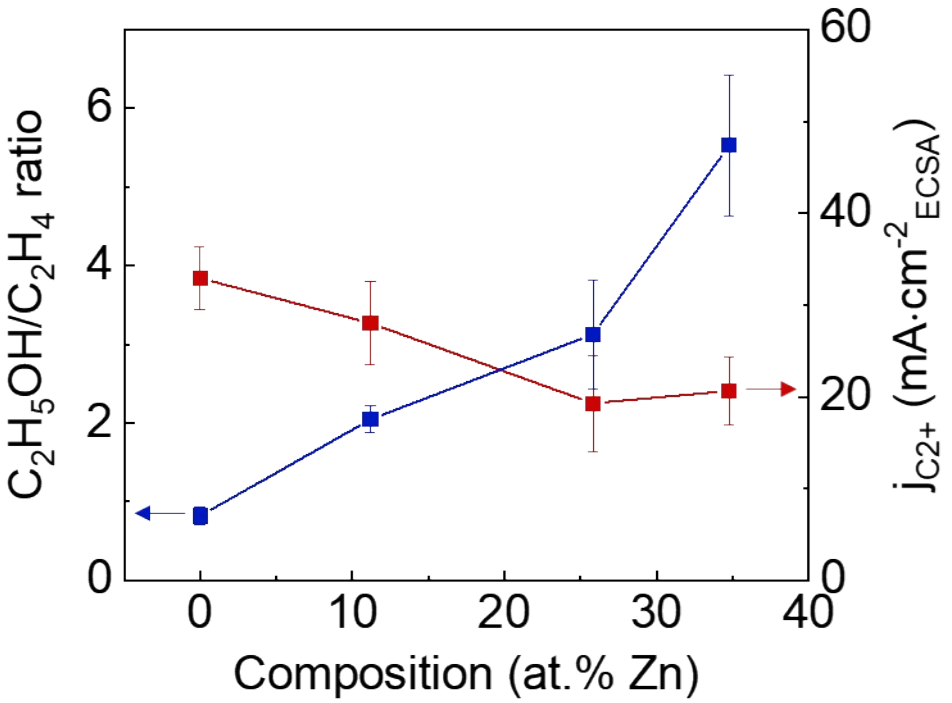

Figure S23. Faradaic efficiencies of products from CO_2RR on Cu, thick Cu and Cu_2Zn_1.The insets are cross-sectional SEM images of each catalyst.

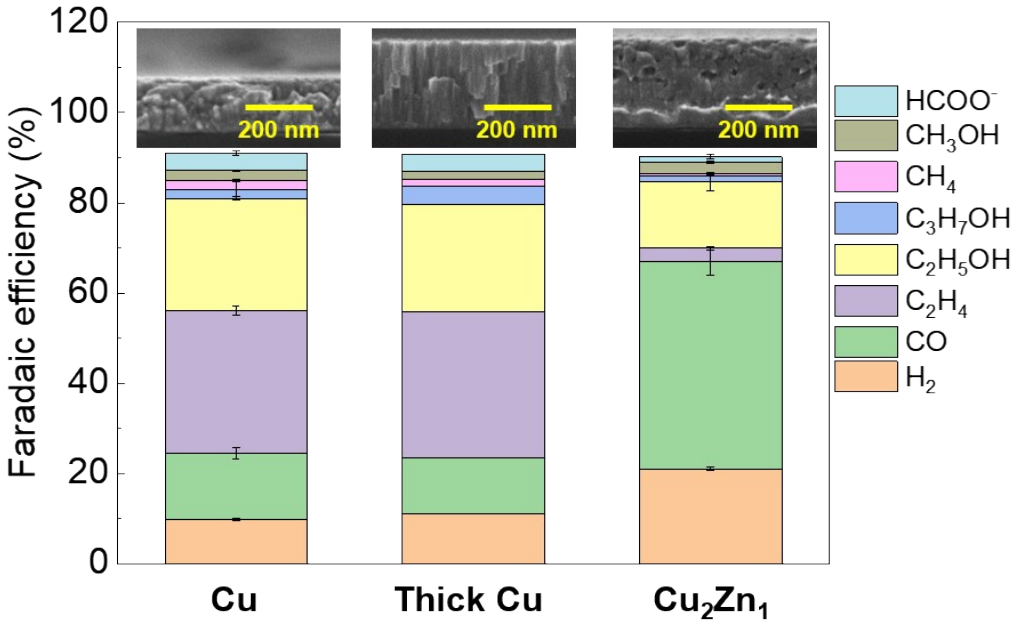

Figure S24. Charge density difference plot of (a) Cu (100), (b) Cu_2Zn_1 (100), (c) Cu (111), (d) Cu_2Zn_1 (111), (e) Cu (110), and (f) Cu_2Zn_1 (110) surfaces with K^+ ion and water layer. The blue region is the electron depletion region, and the yellow region is the electron accumulation region.

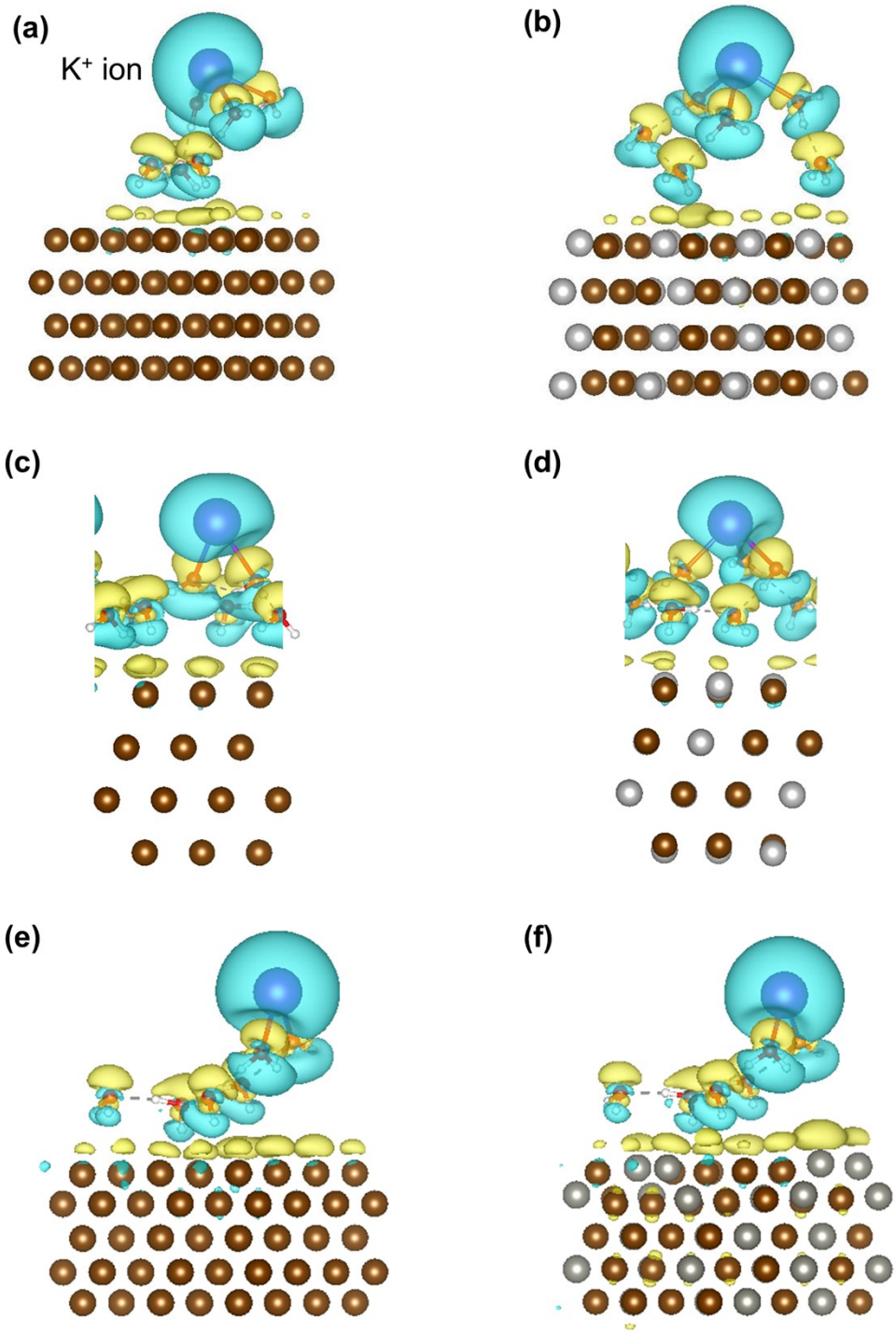

Figure S25. CO binding energy on different sites of (a) Cu_2Zn_1 (100), (b) Cu_2Zn_1 (111), and (c) Cu_2Zn_1 (110) surfaces. Blue spots represent CO adsorption sites. The brown, gray, black, red, white, and purple spheres represent Cu, Zn, C, O, H, and K, repectively.

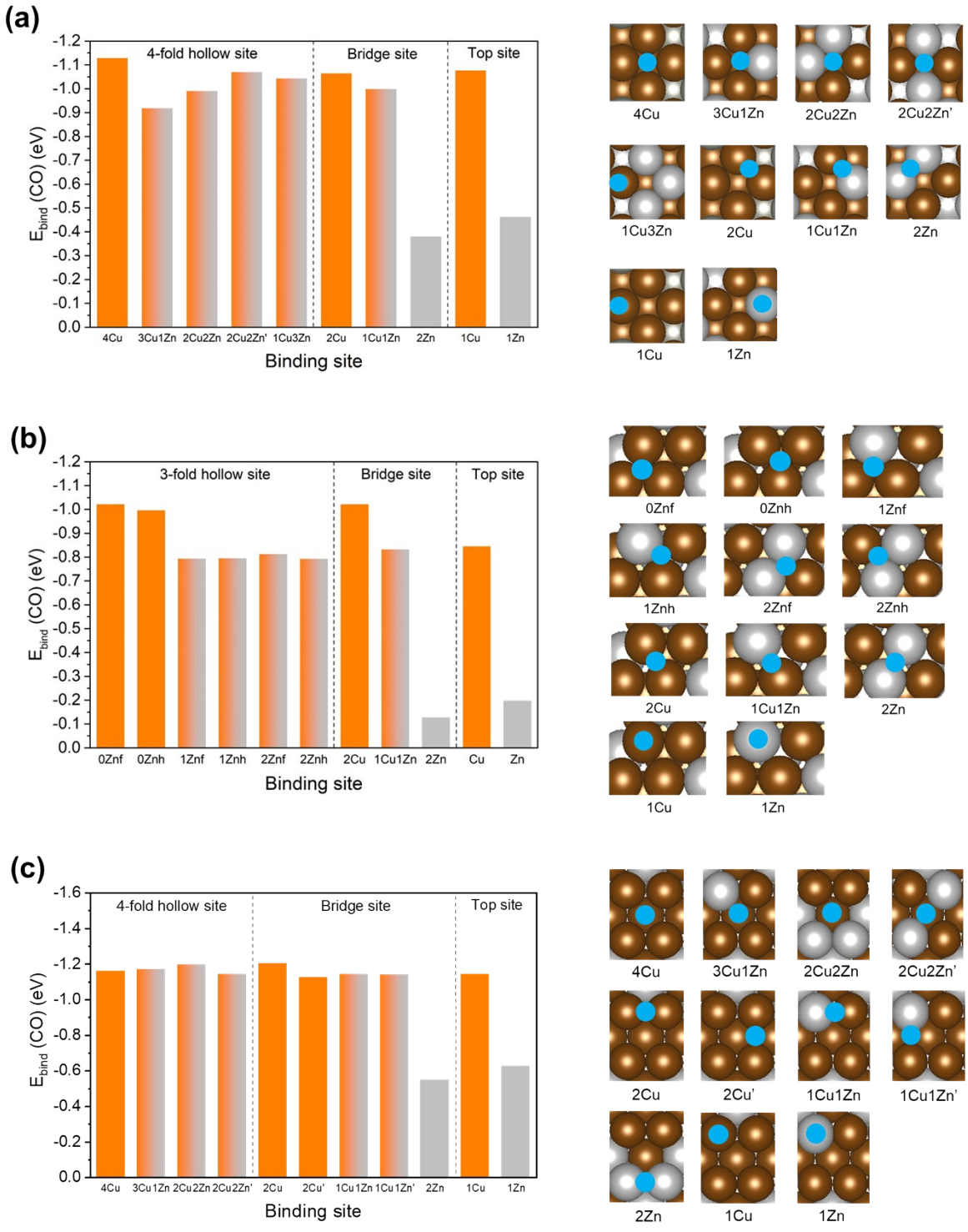

Figure S26. Atomic structure change in CO_2RR on the Cu (100) surface. The numbers on top of each box correspond to the reaction coordinate in Figure 4a. The reaction steps shown in black, blue, and red boxes are the reaction steps of the common pathway, ethylene pathway, and ethanol pathway in Figure 4a, respectively. The brown, black, red, white, and purple spheres represent Cu, C, O, H, and K, repectively.

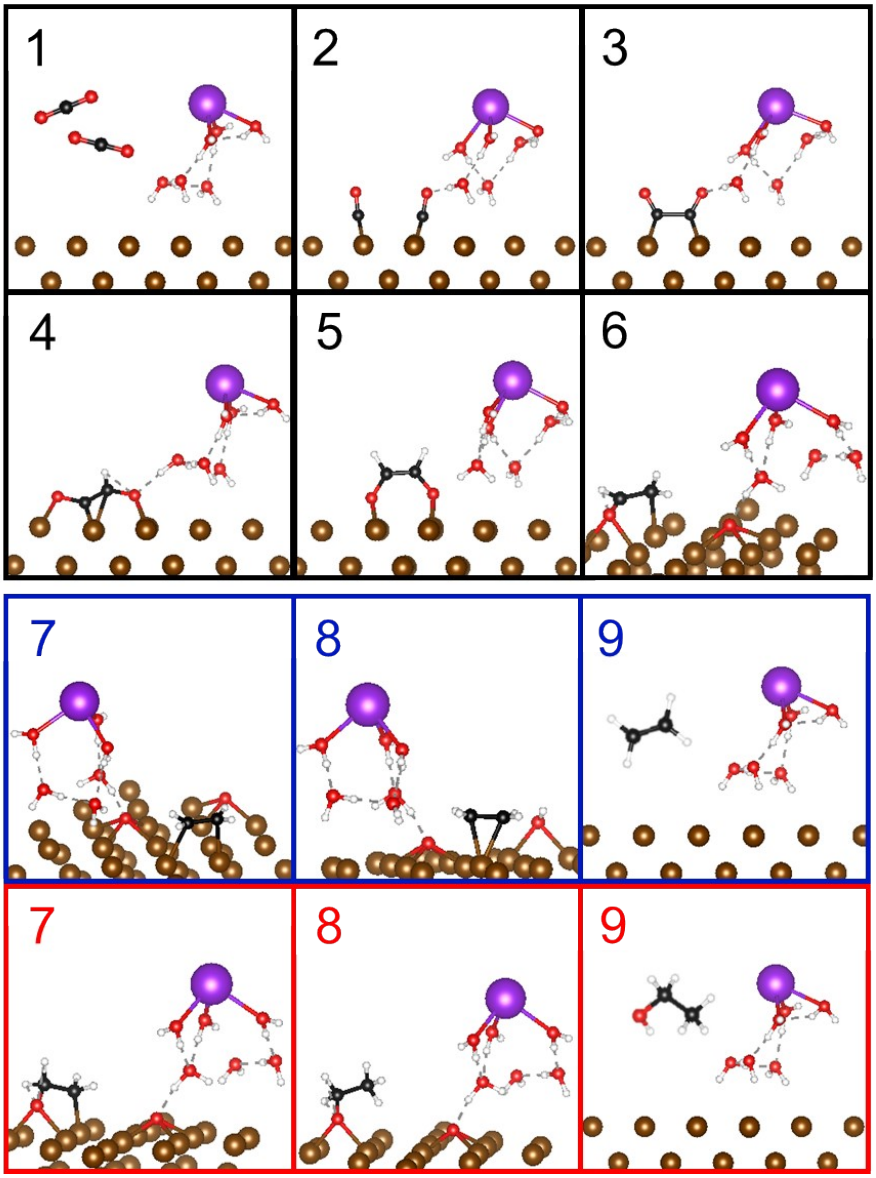

Figure S27. Atomic structure change in CO_2RR on the Cu (111) surface. The numbers on top of each box correspond to the reaction coordinate in Figure 4b. The reaction steps shown in black, blue, and red boxes are the reaction steps of the common pathway, ethylene pathway, and ethanol pathway in Figure 4b, respectively. The brown, black, red, white, and purple spheres represent Cu, C, O, H, and K, respectively.

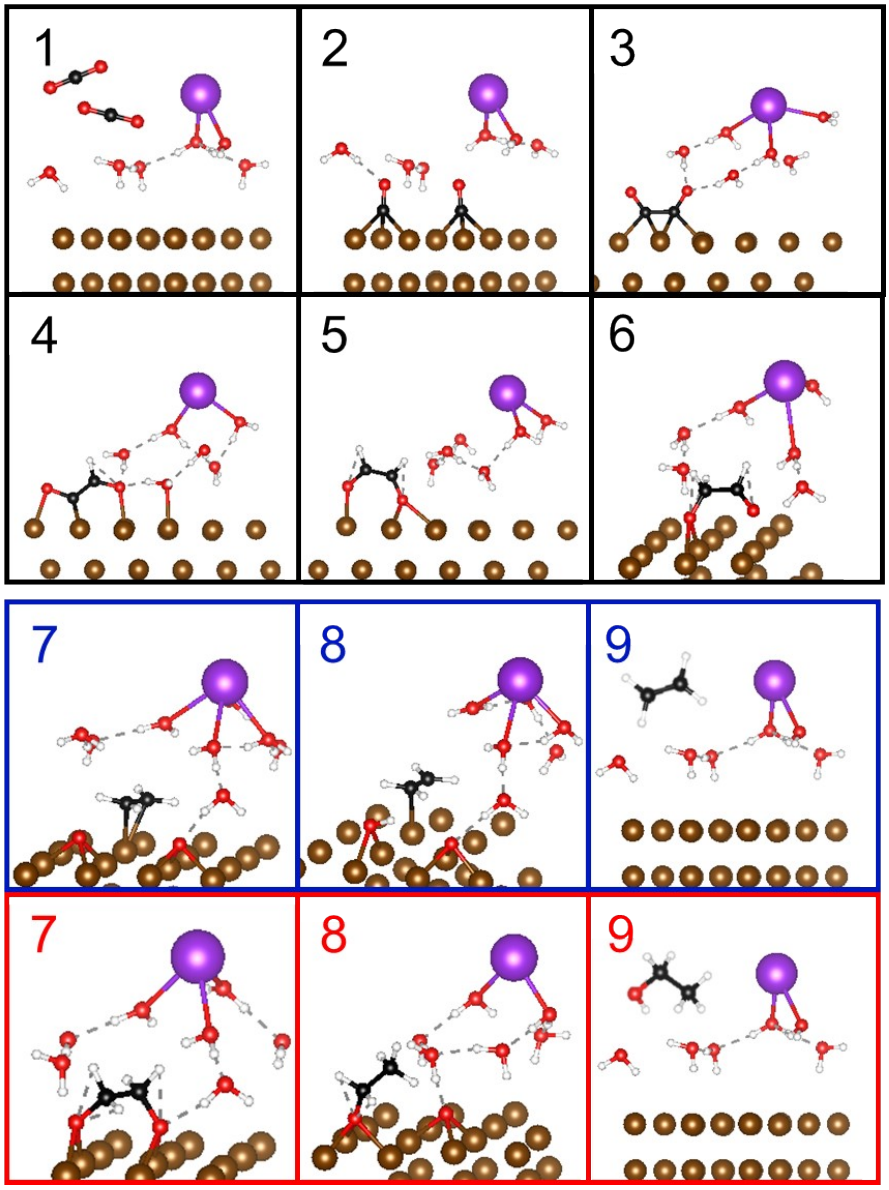

Figure S28. Atomic structure change in CO_2RR on the Cu (110) surface. The numbers on top of each box correspond to the reaction coordinate in Figure 4c. The reaction steps shown in black, blue, and red boxes are the reaction steps of the common pathway, ethylene pathway, and ethanol pathway in Figure 4c, respectively. The brown, black, red, white, and purple spheres represent Cu, C, O, H, and K, respectively.

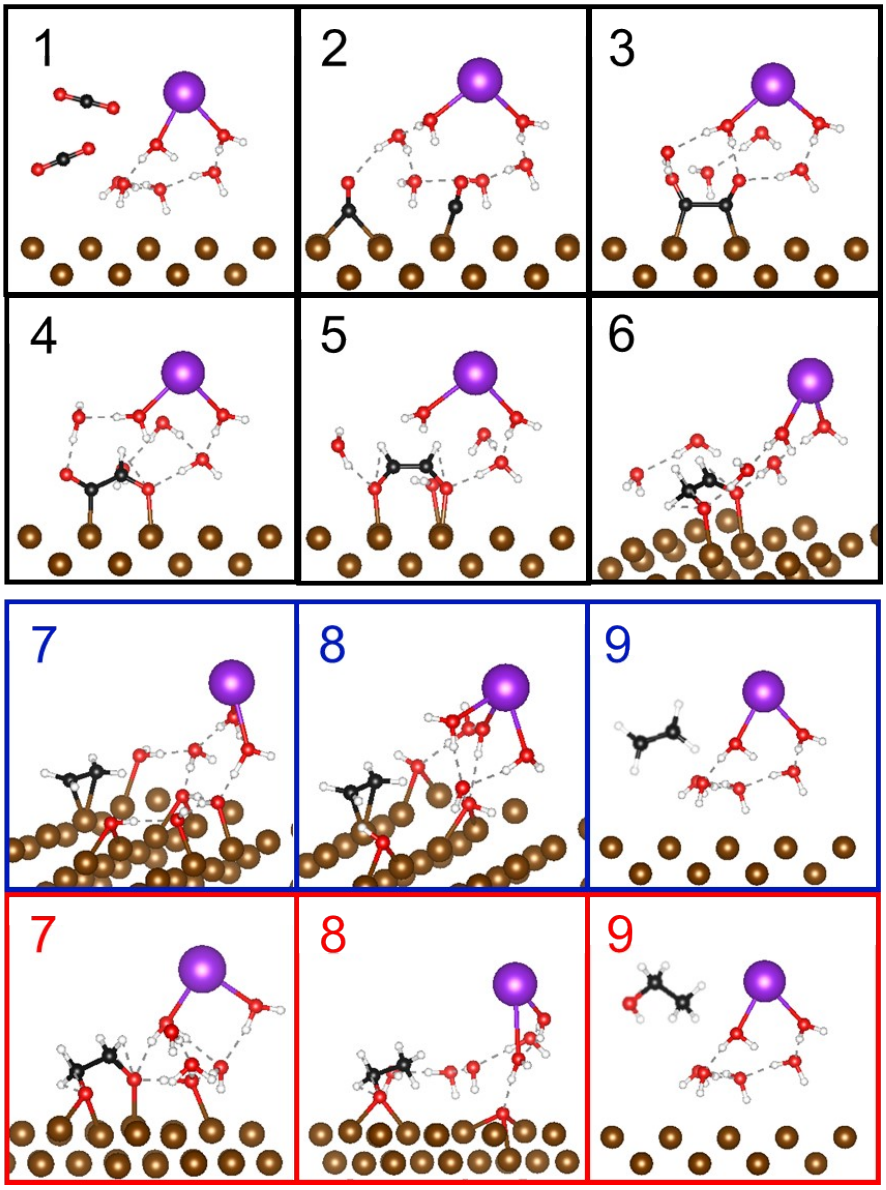

Figure S29. Atomic structure change in CO_2RR on the Cu_2Zn_1 (100) surface. The numbers on top of each box correspond to the reaction coordinate in Figure 4d. The reaction steps shown in black, blue, and red boxes are the reaction steps of the common pathway, ethylene pathway, and ethanol pathway in Figure 4d, respectively. The brown, gray, black, red, white, and purple spheres represent Cu, Zn, C, O, H, and K, respectively.

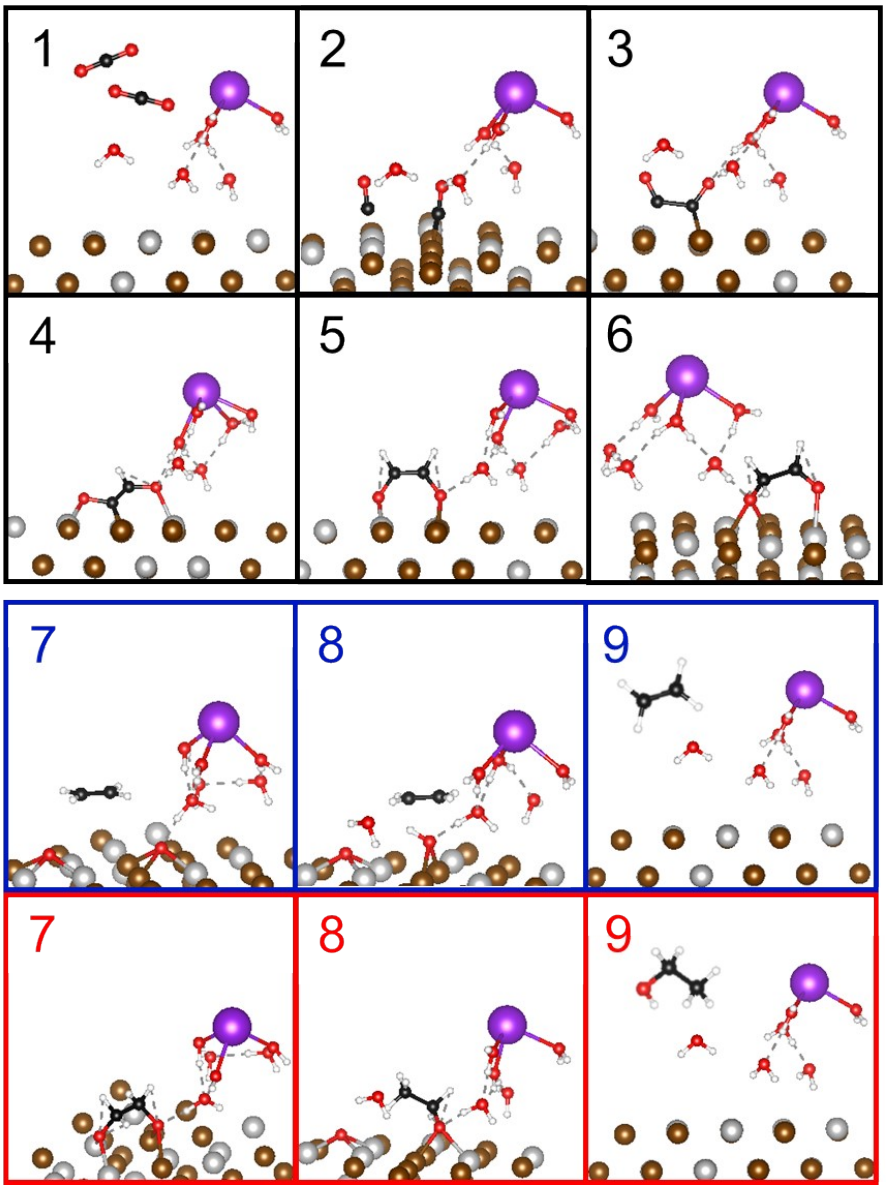

Figure S30. Atomic structure change in CO_2RR on the Cu_2Zn_1 (111) surface. The numbers on top of each box correspond to the reaction coordinate in Figure 4e. The reaction steps shown in black, blue, and red boxes are the reaction steps of the common pathway, ethylene pathway, and ethanol pathway in Figure 4e, respectively. The brown, gray, black, red, white, and purple spheres represent Cu, Zn, C, O, H, and K, repectively.

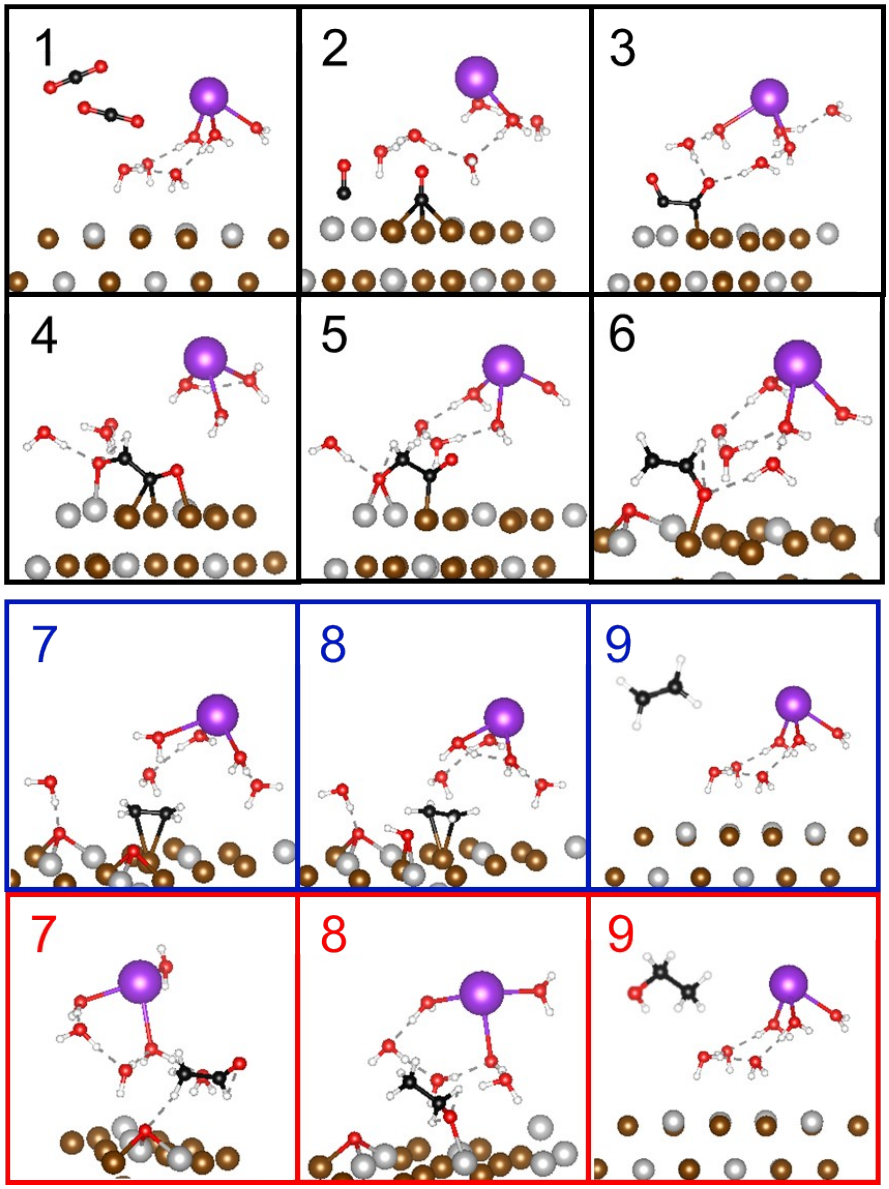

Figure S31. Atomic structure change in CO_2RR on the Cu_2Zn_1 (110) surface. The numbers on top of each box correspond to the reaction coordinate in Figure 4f. The reaction steps shown in black, blue, and red boxes are the reaction steps of the common pathway, ethylene pathway, and ethanol pathway in Figure 4f, respectively. The brown, gray, black, red, white, and purple spheres represent Cu, Zn, C, O, H, and K, respectively.

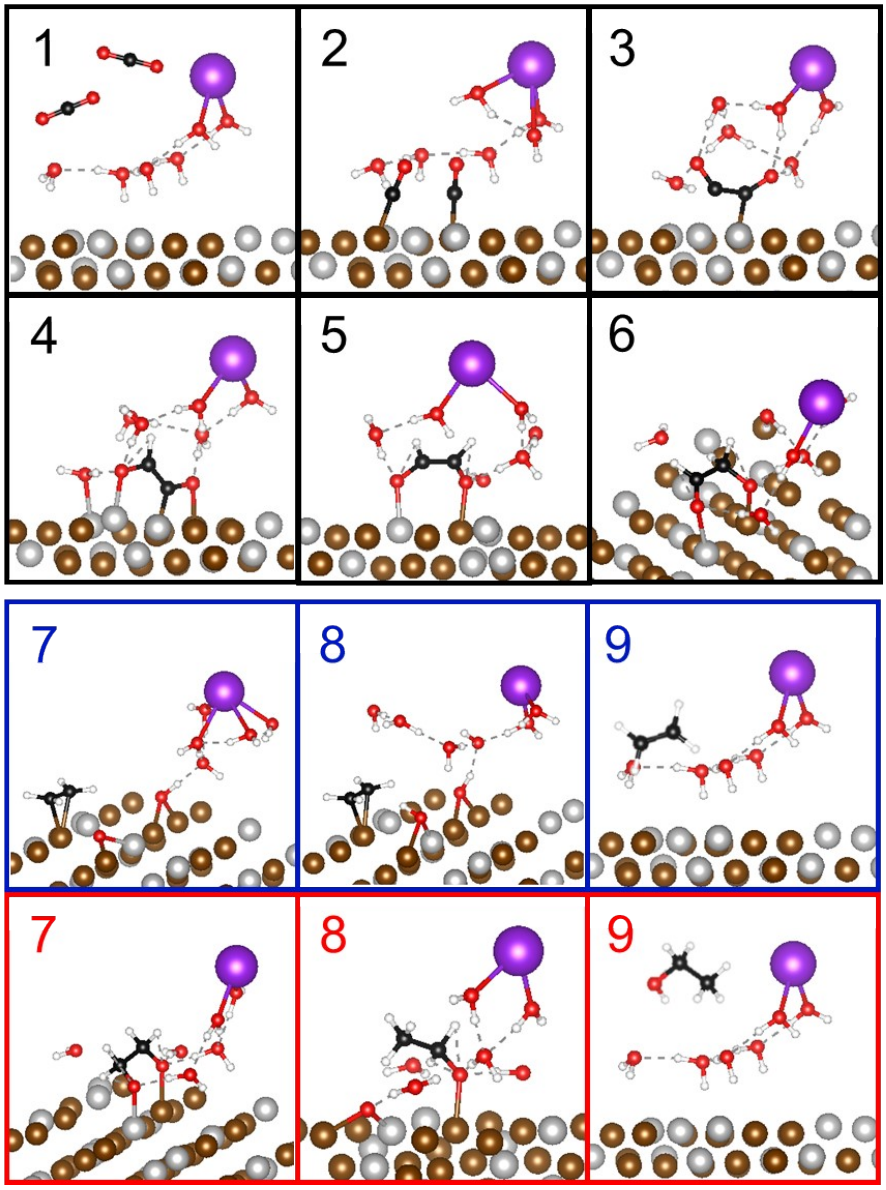

Figure S32. Faradaic efficiency of ethanol from CO_2RR on Cu_9Zn_1/polytetrafluoroethylene (PTFE).

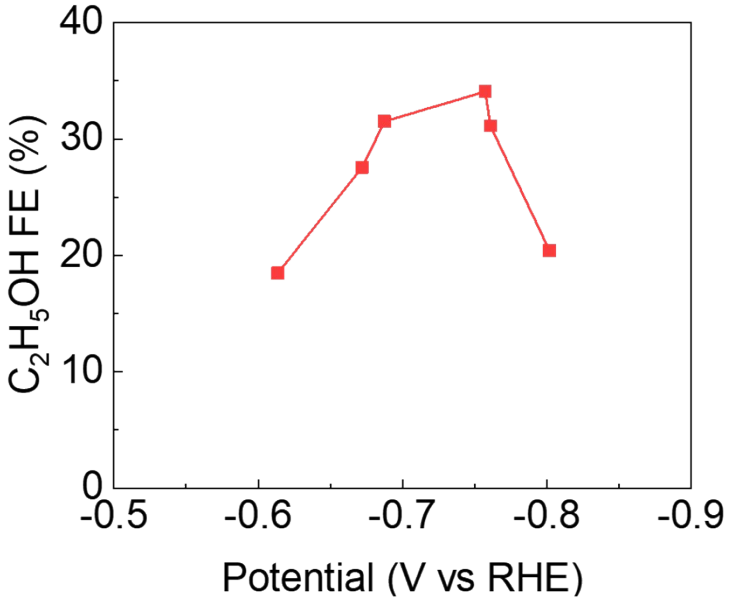

Figure S33. (a) Double-layer capacitance from linear fitting between current density and scan rate on Cu_9Zn_1 on carbon paper and PTFE. (b) SEM images of Cu_9Zn_1 on PTFE and carbon paper. Zn composition was analyzed by SEM-EDS mapping.

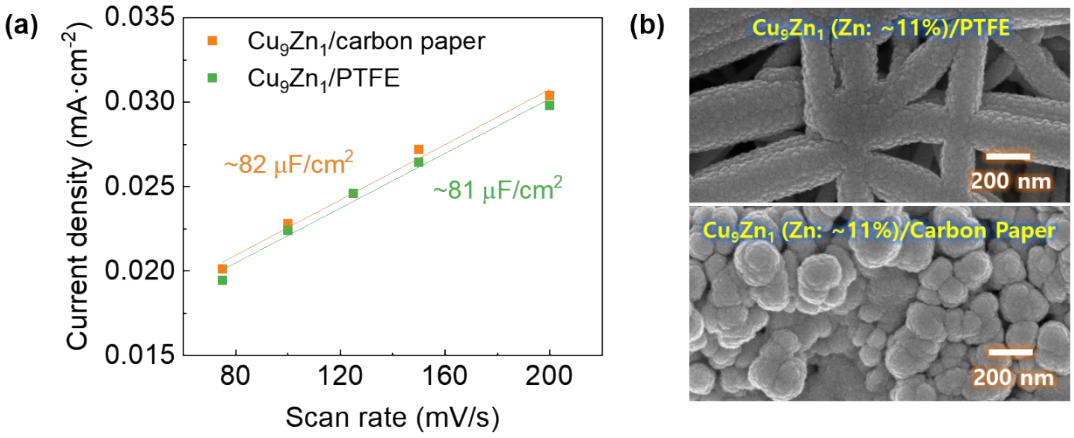

Figure S34. (a) Faradaic efficiencies, (b) current densities, and (c) reaction rates of ethanol as a function of potential, in comparison with other reports with CuZn catalysts. [7-12]

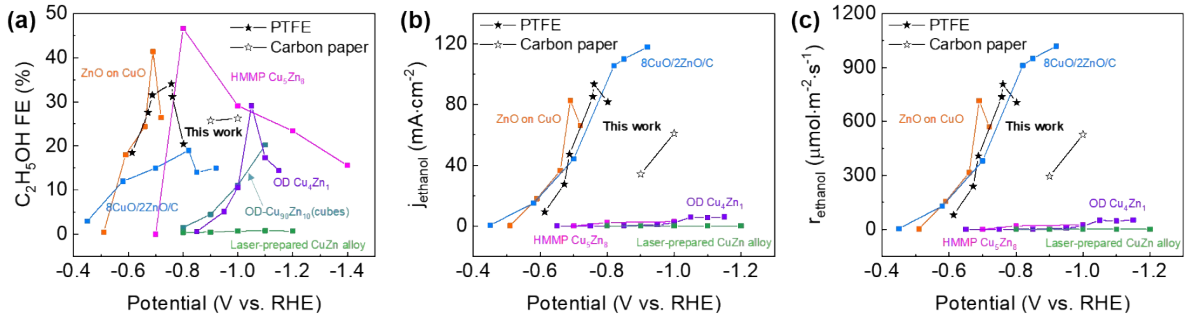

Figure S35. Full-cell energy efficiency of ethanol as a function of time from the stability test of CO_2RR on Cu_9Zn_1/PTFE over 7 h in a membrane electrode assembly (MEA) system.

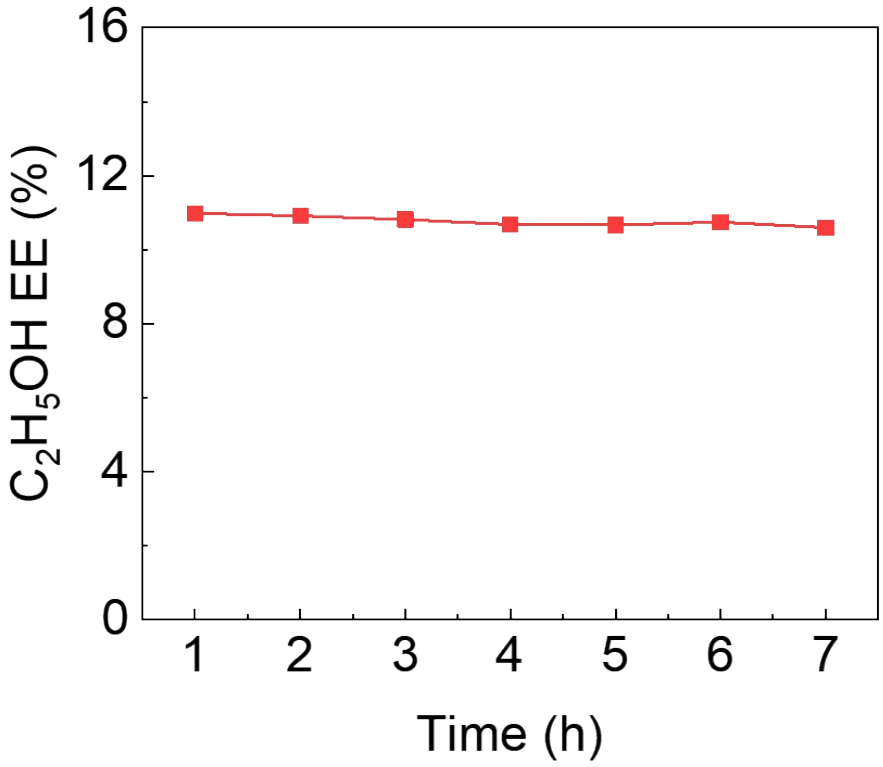

Figure S36. (a) SEM image of Cu_9Zn_1/PTFE and SEM-EDS mapping of (b) CuZn overlap, (c) Cu, and (d) Zn elements of Cu_9Zn_1/PTFE after stability test. Zn composition was analyzed by SEM-EDS mapping.

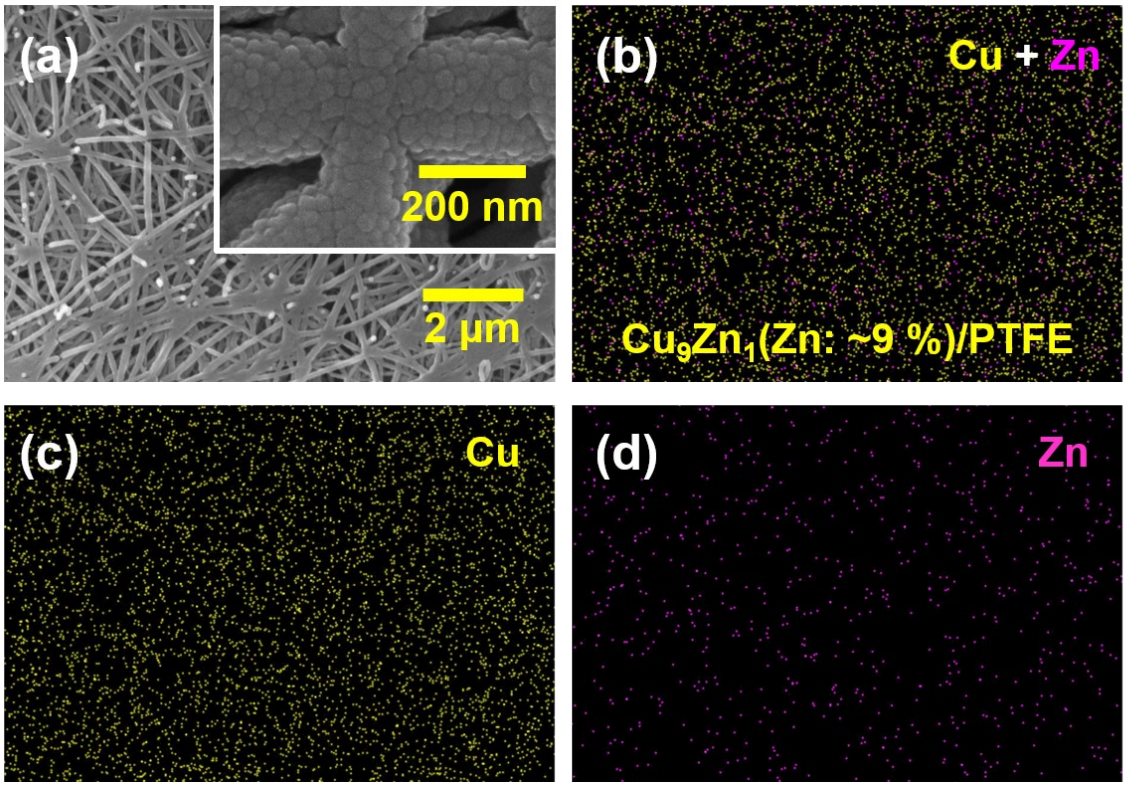

Figure S37. Voltage and faradaic efficiencies as a function of time from the stability test of CO_2RR on Cu_2Zn_1/PTFE over 7 hours in a MEA system.

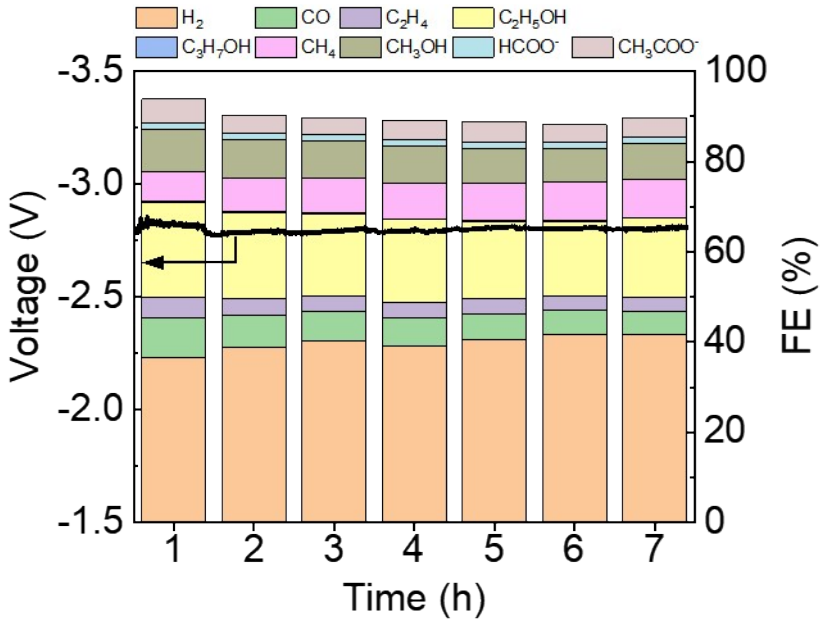

References

1 J. P. Perdew, K. Burke and M. Ernzerhof, Phys. Rev. Lett., 1996, **77**, 3865-3867.
2 G. Kresse and J. Furthmüller, Phys. Rev. B, 1996, **54**, 11169.
3 G. Kresse and J. Furthmüller, Comput., 1996, **6**, 15-50.
4 S. Grimme, J. Comput. Chem., 2006, **27**, 1787-1799.
5 J. K. Nørskov, J. Rossmeisl, A. Logadottir, L. Lindqvist, J. R. Kitchin, T. Bligaard and H. Jónsson, J. Phys. Chem. B, 2004, **108**, 17886-17892.
6 A. A. Peterson, F. Abild-Pedersen, F. Studt, J. Rossmeisl and J. K. Nørskov, Energy Environ. Sci., 2010, **3**, 1311-1315.
7 D. Ren, J. Gao, L. Pan, Z. Wang, J. Luo, S. M. Zakeeruddin, A. Hagfeldt and M. Grätzel, Angew. Chem. Int. Ed., 2019, **58**, 15036-15040.
8 D. Ren, B. S.-H. Ang and B. S. Yeo, ACS Catal., 2016, **6**, 8239-8247.
9 Y. Feng, Z. Li, H. Liu, C. Dong, J. Wang, S. A. Kulinich and X. Du, Langmuir, 2018, **34**, 13544-13549.
10 A. H. da Silva, S. J. Raaijman, C. S. Santana, J. M. Assaf, J. F. Gomes and M. T. Koper, J. Electroanal. Chem., 2021, **880**, 114750.
11 Z. Li, R. M. Yadav, L. Sun, T. Zhang, J. Zhang, P. M. Ajayan and J. Wu, Appl. Catal. A: Gen., 2020, **606**, 117829.
12 X. Su, Y. Sun, L. Jin, L. Zhang, Y. Yang, P. Kerns, B. Liu, S. Li and J. He, Appl. Catal. B, 2020, **269**, 118800.